

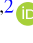



Accuracy evaluation of primary frequency standard NIST-F4

Vladislav Gerginov^{1,*} , Gregory W Hoth¹, Thomas P Heavner¹, Thomas E Parker¹ , Kurt Gibble^{1,2}  and Jeff A Sherman¹ 

¹ National Institute of Standards and Technology, 325 Broadway St, Boulder, CO 80305, United States of America

² Department of Physics, The Pennsylvania State University, University Park, PA 16802, United States of America

E-mail: vladislav.gerginov@nist.gov

Received 31 December 2024, revised 24 March 2025

Accepted for publication 1 April 2025

Published 15 April 2025



Abstract

This work describes the apparatus for NIST-F4, an updated cesium atomic fountain at the National Institute of Standards and Technology (NIST), and presents an accuracy evaluation of the fountain as a primary frequency standard. The fountain uses optical molasses to laser cool a cloud of cesium atoms and launch it vertically in a fountain geometry. In high-density mode, the fractional frequency stability of NIST-F4 is $\sigma_y(\tau) = 1.5 \times 10^{-13} / \sqrt{\tau}$, where τ is the measurement time in seconds. The short-term stability is limited by quantum projection noise and by phase noise from the local oscillator, an oven-controlled crystal oscillator operating at 5 MHz. Systematic frequency shifts and their uncertainties have been evaluated, resulting in a systematic (type B) fractional frequency uncertainty $\sigma_B = 2.2 \times 10^{-16}$.

Keywords: cesium fountain, primary frequency standard, microwave atomic clock

1. Introduction

Cesium fountain primary frequency standards (PFSs) have calibrated the base unit of time for the International System of Units (SI) and International Atomic Time (TAI) for over two decades [1]. These devices have been constructed in many national metrology institutes [2–17], with type B fractional frequency uncertainties at the low- 10^{-16} level [6–8, 10, 11, 15, 18]. Accurate cesium fountains are essential for comparisons with optical frequency standards, in anticipation of a revision to the SI definition of the second [19], and they are expected to significantly contribute to local and international time-keeping and frequency calibration for years to come.

Previously, the National Institute of Standards and Technology (NIST) has developed several cesium fountain PFSs [4, 6, 20]. Here, we describe the design, operation, performance and a first accuracy evaluation of an updated cesium fountain, NIST-F4. This fountain incorporates many components of NIST-F1, which was decommissioned in 2022 [4, 20]. The outline of this manuscript is as follows. Section 2 describes the physics package of NIST-F4. Section 3 summarizes the fountain's laser systems, microwave synthesis, and control systems. Section 4 presents the evaluation of the main fountain frequency shifts and the uncertainty budget. Section 5 considers additional sources of frequency shifts. Section 6 reports the results of several measurement campaigns to compare NIST-F4 with other cesium fountain PFSs. Finally, section 7 concludes the paper and discusses the outlook for NIST-F4.

2. Design of the physics package

The physics package of NIST-F4 uses many components of the vacuum system from NIST-F1 [4, 20] and features a new set

* Author to whom any correspondence should be addressed.



Original Content from this work may be used under the terms of the [Creative Commons Attribution 4.0 licence](https://creativecommons.org/licenses/by/4.0/). Any further distribution of this work must maintain attribution to the author(s) and the title of the work, journal citation and DOI.

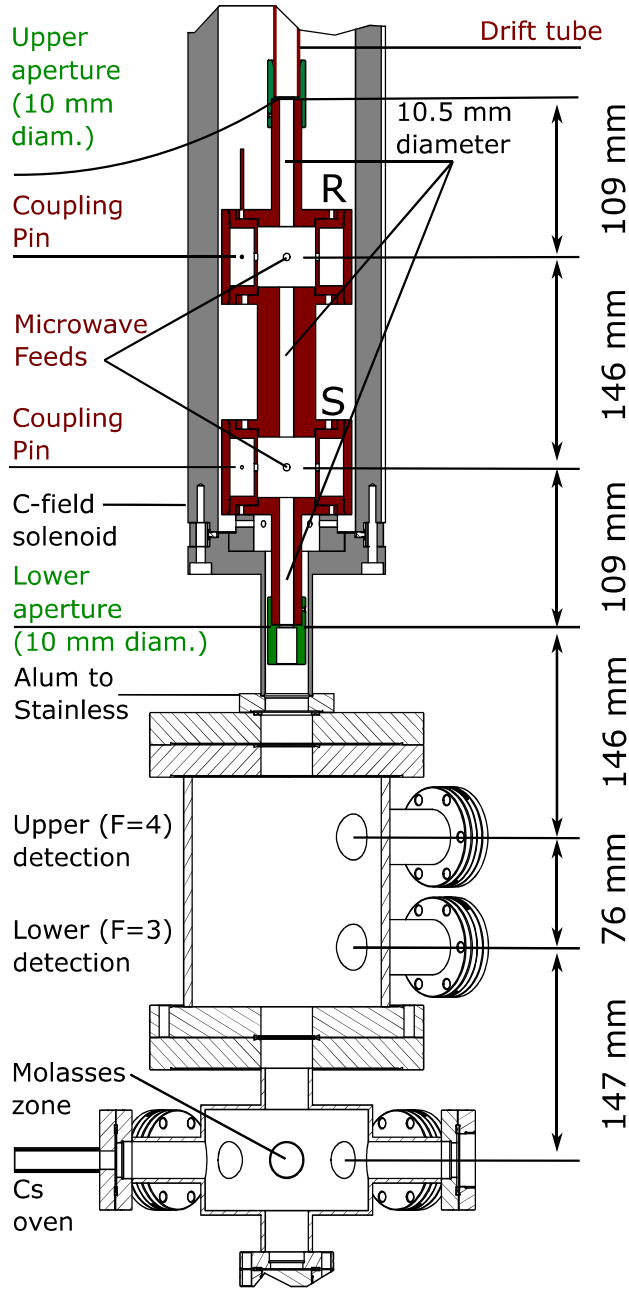


Figure 1. Schematic diagram of the molasses zone, the detection region, and the microwave cavities for NIST-F4. Cavity structures are shown in red; restrictive apertures are shown in green. Gray shaded regions indicate the aluminum UHV chamber. Hatched regions indicate the stainless steel vacuum chambers. The labels R and S indicate the Ramsey and state-selection microwave cavities. The vacuum is maintained by an ion pump attached to the molasses region and by non-evaporable getter pumps (NEGs) mounted at the top of the vacuum system.

of state-selection and Ramsey microwave cavities. A structural diagram is shown in figure 1. Selected parameters of the NIST-F4 physics package are given in table 1.

At the bottom of the fountain, stainless-steel vacuum chambers provide optical access for loading atoms into optical

Table 1. Selected parameters of the NIST-F4 physics package. h_S and h_R give the distance between the mid-plane of the state-selection and Ramsey cavities and the cooling zone. $T_{S,up}$, $T_{R,up}$, and $T_{R,down}$ are the times after launch when the atom cloud crosses the mid-plane of each cavity during the fountain sequence. The gravitational acceleration was measured at marker DR9959 in the NIST-F4 laboratory [21]. Δt_{Rabi} is the time required for the cloud to cross from endcap to endcap in the Ramsey cavity.

Parameter	Value	Units
Internal cavity radius	21.50	mm
Internal cavity height	42.62	mm
Loaded Q -factor (Ramsey)	28×10^3	—
TM ₁₁₁ filter height	5.00	mm
TM ₁₁₁ filter width	0.60	mm
h_S mid-plane	0.479	m
h_R mid-plane	0.624	m
Gravity acceleration	9.796 023 73(4)	$m s^{-2}$
Cloud launch velocity	4.330	$m s^{-1}$
$T_{S,up}$	130	ms
$T_{R,up}$	181	ms
$T_{R,down}$	703	ms
Δt_{Rabi}	16.71	ms

molasses, polarization-gradient cooling, as well as launching and detecting the atoms. Cesium vapor is supplied by a heated copper tube containing an ampoule of Cs metal. Above the detection region, a vacuum flange adaptor connects the stainless steel chambers to an ultrahigh vacuum (UHV) aluminum chamber, which contains the new copper state-selection (S) and Ramsey (R) microwave cavities. The two microwave cavities are nominally identical, and their design will be described in more detail in a separate paper [22]. Below the state-selection cavity and above the Ramsey cavity, apertures with a 10 mm diameter truncate the atomic cloud at the end of the cutoff tubes and prevent the atomic trajectories from passing close to the edge of the apertures in the cavity end-caps, which have a diameter of 10.5 mm. Above the Ramsey cavity, the atoms are enclosed by a drift tube, a long, below-cutoff copper tube with an inner diameter of 13 mm, to suppress microwave leakage frequency shifts during the Ramsey free evolution period [4, 6].

A three-layer magnetic shield is mounted outside of the aluminum vacuum chamber. Inside the shielded region, a coil wound around the outer cylindrical wall of the aluminum vacuum chamber generates the bias magnetic field for fountain operation (C-field). The coil is held in a groove machined onto the chamber wall. Near the center of the coil, the groove has approximately 157.5 turns per meter (four threads per inch). The pitch increases by a factor of two at the ends of the cylindrical chamber, for about 20 mm, to improve the homogeneity of the C-field close to the ends of the shielded region. The return path for the coil wire is a vertical groove machined into the cylindrical wall of the aluminum chamber.

These grooves also house a heater that controls the temperature of the aluminum chamber and keeps the Ramsey cavity on resonance. Heater wire is wound around the aluminum chamber such that the forward and return currents propagate in

close proximity to suppress magnetic fields generated by the 15 kHz AC heating current.

An isolated transformer is used to avoid the generation of DC magnetic field by the heater. The proximity of the heater's forward and return wires assures a small AC magnetic field. The residual AC magnetic field is sufficiently suppressed by the 19 mm thick aluminum vacuum enclosure and the skin depth effect; the skin depth in aluminum at 15 kHz is <0.7 mm. The AC current is continuously supplied to maintain the temperature of the drift tube around 5 K above room temperature while avoiding microwave phase transients synchronous with the fountain cycle. The temperature is measured with a calibrated, in-vacuum platinum resistance element (PT100 sensor) mounted on the drift tube 100 mm above the atomic apogee. The PT100 resistance is probed in a 4-wire configuration once every 5 min by a computer that is not synchronized with the fountain cycle. During a measurement campaign, the sensor activations are randomly distributed with respect to the fountain spectroscopy cycle so that any electronic disturbances should average to zero. The probe current is applied only during the ~ 1 s long measurement.

3. Laser setup, microwave synthesizer, and experimental control

3.1. Laser setup

The optical systems of NIST-F4 are largely inherited from NIST-F1 [4, 20]. Since these systems have been described previously, they are only briefly summarized here. Light for cooling, launching, and detecting the Cs atoms is produced with a Ti:Sapphire laser that is frequency-stabilized using cesium vapor cell spectroscopy. Repumping light is produced from a distributed Bragg reflector diode laser, which is also frequency-stabilized using cesium vapor cell spectroscopy. Figure 2 shows a schematic diagram of the laser system, and the network of acousto-optic modulators (AOMs) used to control the beams required for fountain operation.

At the base of the fountain physics package, cold atoms are produced with $\text{lin}\perp\text{lin}$ optical molasses in the (0,0,1) geometry [4]. The horizontal molasses beams have a diameter of 25 mm ($1/e^2$), and the vertical beams have a diameter of 15 mm ($1/e^2$). The downward beam is aligned geometrically to propagate along the vertical fountain axis. After the beam passes through the fountain structure, a camera is used to verify its alignment. The upward beam is coupled into the optical fiber delivering the downward beam to assure the beams counter propagate and overlap. The residual misalignment between the upward and downward beams is less than 1 mrad.

At the beginning of each fountain cycle, cold atoms are loaded into the optical molasses. For high-density mode, the loading time is about 500 ms. After loading, the atoms are accelerated upward by linearly ramping the frequency of the vertical molasses beams by 5.1 MHz over 1 ms. Then, all molasses beam are ramped down by 44 MHz over 1.5 ms.

At the same time, the intensity of the molasses beams is reduced. The post-cooling sequence is experimentally optimized to maximize the number of atoms reaching the detection at the end of each fountain cycle. In the detection zones, fluorescence from the atomic cloud is collected onto large-area ($10\text{ mm}^2 \times 10\text{ mm}^2$) photodiodes. The signals are amplified by low-noise transimpedance amplifiers and recorded by the control computer.

The beams used to excite the atomic fluorescence propagate horizontally, oriented at 45° with respect to the cavity feed axes. They have a horizontal width of 25 mm and a vertical height of 2 mm. The intensity distribution of the detection beams in the horizontal direction is homogeneous to better than 90%. These beams are retro-reflected using quarter ($\lambda/4$) waveplates and flat mirrors so that the returning beams have orthogonal linear polarizations. They are red-detuned by 0.25 MHz from the cycling transition, and their intensity is stabilized. Atoms in the $|F = 4\rangle$ state are detected in the upper zone shown in figure 1 and then pushed away by an additional beam which is not retro-reflected. Then, atoms in the $|F = 3\rangle$ state are optically pumped to $|F = 4\rangle$ and detected in the lower zone.

3.2. Microwave synthesizer

The Ramsey microwave synthesizer of NIST-F4 is described in detail in [23] and is only briefly summarized here. The 5 MHz output of an oven-stabilized crystal oscillator (OCXO), with a fractional frequency instability of approximately 1×10^{-13} at 1 s averaging time, is multiplied to 10 MHz and 100 MHz. A phase-locked loop (PLL) locks the 100 MHz signal derived from the OCXO to a 100 MHz signal from a hydrogen maser. The PLL loop filter time constant is approximately 100 s. A dielectric resonator oscillator (DRO) operating at 9.2 GHz is phase-locked to this OCXO. At short times, the phase noise of the DRO's microwave signal is limited by the OCXO. At longer averaging times, the DRO's frequency is determined by the hydrogen maser. To reduce spurs in the microwave spectrum related to the power line, the DC power for the synthesizer is delivered from trickle-charged batteries.

A direct digital synthesizer (DDS), referenced to the 10 MHz OCXO-derived output, fine tunes the frequency of the microwave signal. A single sideband mixer combines the DDS signal near 7.368 MHz with the 9.2 GHz output of the DRO to generate 9.192 GHz. The DDS selectively detunes the microwaves during each fountain cycle with frequency shift keying (FSK) modulation. To suppress frequency shifts due to microwave leakage as the atoms descend through the fountain, the microwaves are detuned by about 900 Hz after the atoms leave the Ramsey cavity [24].

The 9.192 GHz synthesizer output is sent to a microwave splitter network, described in detail in [25], which drives the four independent feeds of NIST-F4's Ramsey cavity. The splitter fine tunes the amplitude and phase of the four independent feeds. Based on single-feed Rabi flopping measurements, the amplitudes of the four feeds are balanced to better than

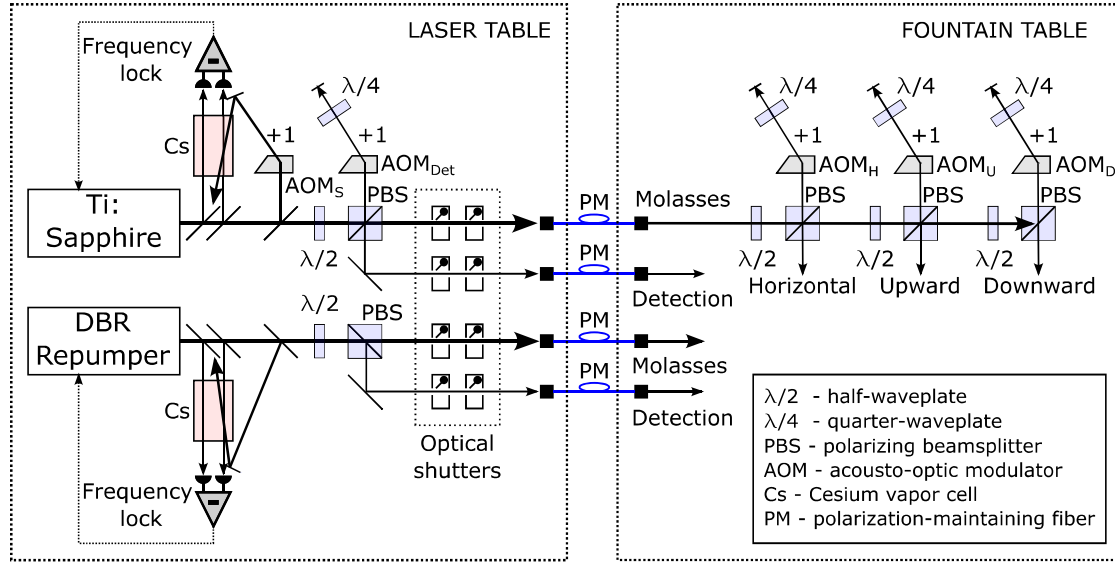


Figure 2. Laser system for NIST-F4 illustrating the light sources for cooling and repumping as well as the AOMs that control the beams required for fountain operation. The system is described in more detail in [4, 20].

1%. By activating different feeds for each Ramsey interaction during the same fountain cycle, the phase differences between the individual feeds are measured and matched to better than 100 μ rad.

An independent synthesizer with essentially the same design drives the state-selection cavity. To suppress potential microwave leakage frequency shifts, a microwave switch attenuates the output of the synthesizer by >45 dB. FSK modulation also detunes the frequency of the state-selection DDS. The state-selection microwaves are only on-resonance and transmitted through the switch during the interval from shortly before the atoms enter the state-selection cavity until just after the atoms enter the cut-off tube between the two cavities.

3.3. Experimental control

The fountain control system uses a commercial hardware platform run by customized control software [26]. Arbitrary waveform generators produce the radio-frequency signals sent to AOM_H, AOM_U, AOM_D and AOM_{Det} in figure 2. A counter/timer module generates the required sequence of logic signals. Analog signals from the fountain detection system are acquired with a 24-bit dynamic signal acquisition module and analyzed by the software for steering the Ramsey DDS frequency. The software logs the frequency steers, which determine the frequency of the microwave signal sent to the Ramsey cavity. During an evaluation campaign, the software cycles between high- and low-density modes, and magnetic field (C-field) mode for interleaved measurements of two of the systematic frequency biases: the quadratic Zeeman shift, and the cold collision shift.

4. Systematic frequency shifts and shift uncertainties

This section describes the systematic frequency shifts of NIST-F4 and their uncertainties. The effects for which a correction is applied, or an uncertainty is evaluated, are summarized in table 2.

4.1. Quadratic Zeeman shift

The magnetic field in the fountain drift zone (C-field) produces a shift of the clock transition frequency. From the Breit–Rabi formula [27], the fractional frequency shift can be expressed as:

$$\frac{\Delta f_{QZ}}{\nu_0} = 8 \left(\frac{f_Z}{\nu_0} \right)^2, \quad (1)$$

where f_Z is the frequency difference between the clock transition frequency ν_0 and the magnetically-sensitive $|F = 3, m_F = -1\rangle \rightarrow |F = 4, m_F = -1\rangle$ microwave transition.

During an evaluation campaign, the fountain measures f_Z a few times each hour by locking the microwave synthesizer frequency to the central Ramsey fringe of the magnetically sensitive transition. Small fluctuations in the C-field over time are the main source of uncertainty in the quadratic Zeeman shift. Typical temporal variations of this shift are shown in figure 3 (blue curve). For this campaign, the average quadratic Zeeman fractional frequency shift was 1369.4×10^{-16} with a standard deviation of 0.14×10^{-16} . The average shift is given as a typical correction in table 2. Based on several measurement campaigns, an uncertainty of 0.20×10^{-16} is assigned in table 2.

Table 2. Fractional frequency corrections and type B uncertainties for systematic effects in NIST-F4, divided by 10^{-16} . The entry for relativistic shifts includes the contributions due to the gravitational red shift and the second-order Doppler shift.

Systematic effect	Correction	Uncertainty
Relativistic shifts	1809.59	0.01
Quadratic Zeeman	1369.4	0.2
Blackbody radiation	−170.4	0.6
Cold collisions	10.0	1.0
Microwave lensing	0.9	$\begin{pmatrix} +0.2 \\ -0.4 \end{pmatrix}$
Distributed cavity phase (DCP):		
DCP ($m = 0$)	0.05	$\begin{pmatrix} +0.02 \\ -0.08 \end{pmatrix}$
DCP ($m = 1$)	0	1.7
X-tilt axis ^a	(0)	(1.4)
Y-tilt axis ^a	(0)	(1.0)
DCP ($m = 2$)	0	0.20
Microwave modulation and spurs	0	0.5
Microwave leakage	0	0.4
Cavity pulling	0	0.11
Rabi and Ramsey pulling	0	0.10
Majorana transitions	0	0.10
Background gas collisions	0	0.03
AC Stark (light)	0	0.01
Total	3019.5	2.2

^a The $m = 1$ DCP shifts and uncertainties along the X- and Y-tilt axes are given for information only, as they are included in quadrature in the DCP ($m = 1$) term.

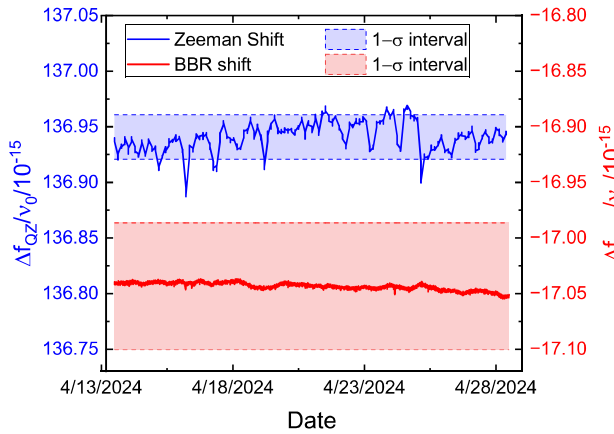


Figure 3. Left axis: quadratic Zeeman fractional frequency shift ($\Delta f_{QZ}/\nu_0$, blue curve). Right axis: blackbody radiation fractional frequency shift ($\Delta f_{BBR}/\nu_0$, red curve). Dashed lines and shaded regions show $1-\sigma$ intervals based on the uncertainty assigned in table 2.

for the temporal variations of the magnetic field. This corresponds to fluctuations of f_Z on the order of 0.1 Hz for NIST-F4's typical value, $f_Z \approx 1203$ Hz.

The inhomogeneity of the C-field along the atomic trajectories is also a potential source of systematic uncertainty

in the quadratic Zeeman shift in two ways. The first possible source of uncertainty arises from the requirement to identify the central Ramsey fringe on the $|F = 3, m_F = -1\rangle \rightarrow |F = 4, m_F = -1\rangle$ transition. In NIST-F4, the central Ramsey fringe for the magnetically sensitive microwave transition is identified by launching the atoms to different heights. For short launch heights, the central Ramsey fringe can be clearly identified [28]. By following this central fringe as the launch height increases, it is possible to map the central fringe frequency, f_Z , as a function of the launch height. The magnetic field, B_m , measured with this mapping procedure is shown as a function of launch height in figure 4 (red symbols).

A second possible source of systematic uncertainty from magnetic inhomogeneities is due to the quadratic dependence of the frequency shift of the clock transition on the magnetic field. When the field is inhomogeneous, the measured, trajectory-averaged value of f_Z does not give the correct value for the clock transition shift via equation (1) because $\langle f_Z \rangle^2 \neq \langle f_Z^2 \rangle$. To quantify this difference, a corrected magnetic field, B_c , is calculated to account for the time the atoms spent at each vertical position in the fountain [29]. The results are shown in figure 4 (solid curve). The error in the quadratic Zeeman shift due to the magnetic field inhomogeneity is determined from $\langle B_c \rangle^2 - \langle B_c^2 \rangle$ [29, 30]. It is approximately 6×10^{-19} , which is negligible.

4.2. Blackbody radiation shift

Blackbody radiation from the environment perturbs the fountain clock transition and produces a frequency shift. The fractional frequency shift can be expressed as [31]:

$$\frac{\Delta f_{BBR}}{\nu_0} = \frac{k_0 E_{300}^2}{\nu_0} \left(\frac{T}{T_0} \right)^4 \left(1 + \epsilon \left(\frac{T}{T_0} \right)^2 \right), \quad (2)$$

where T is the ambient temperature in kelvin, $T_0 = 300$ K, $E_{300} = 831.9$ V m^{−1} is the root-mean-square (rms) blackbody radiation electric field at 300 K, $k_0 = -2.282(4) \times 10^{-10}$ Hz (V m^{−1})^{−2} [33], $\epsilon = 0.013(1)$ [34], and ν_0 is the Cs transition frequency.

The ambient temperature is measured with the calibrated, in-vacuum PT100 sensor mounted on the drift tube as described in section 2. The temperature sensor is also used to determine the heater current required to keep the Ramsey cavity resonant with 9.192 GHz. The operating temperature is approximately 298 K.

Typical fractional frequency shifts due to blackbody radiation are shown in figure 3 (red curve) for a 15 days fountain evaluation interval. The shifts are estimated from the measured resistance of the PT100 sensor and equation (2). A conservative temperature measurement uncertainty of 0.2 K is assumed that includes the 0.05 K sensor accuracy uncertainty. After combining the 0.2 K temperature measurement uncertainty with the uncertainties of k_0 and ϵ , the resulting uncertainty in the blackbody radiation shift is 0.6×10^{-16} . It is included in table 2 with a typical correction.

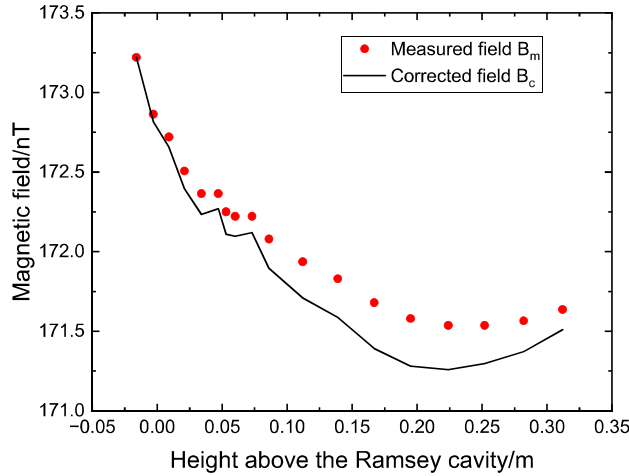


Figure 4. Magnetic field as a function of height above the mid-plane of the Ramsey cavity. B_m (red symbols) is the field estimated from measurements of f_Z during the field mapping procedure. B_c (solid curve) is an estimate of the field corrected for the amount of time the atoms spent at each vertical position in the fountain [29]. The magnetic field is calculated from f_Z as $B \approx f_Z / (2 \times 3.5 \text{ Hz nT}^{-1})$ [32].

The thermal environment of the atoms is mostly determined by the temperature of the Ramsey cavity and the drift tube, which is approximately 5 K above the lab temperature. The atoms are exposed to room-temperature blackbody radiation through the aperture below the state-selection cavity (diameter 10 mm) and the aperture at the top of the drift tube (diameter 13 mm). The solid angles subtended by these apertures while the atoms are above the Ramsey cavity are small, and the resulting correction to the blackbody radiation shift is less than 1×10^{-18} , which is neglected.

4.3. Relativistic red and second-order Doppler shifts

The fractional relativistic red shift experienced by a clock at a point P above the geoid is [35]:

$$\frac{\Delta f}{f} = \frac{f_P - f_0}{f_0} = -\frac{C_P}{c^2}, \quad (3)$$

where C_P is the geopotential number at point P , and c is the speed of light. The reference point for the red shift calculation is geodesy marker DR9599 located on the floor of NIST-F4's laboratory. The geopotential number for the DR9599 marker is $C_{\text{DR9599}} = 16243.68(0.02) \text{ m}^2 \text{ s}^{-2}$ [21], resulting in a fractional frequency shift of 1807.35×10^{-16} with an uncertainty of 2×10^{-19} relative to the geoid.

The mid-plane of NIST F4's Ramsey cavity is $h_m = 1.943(5) \text{ m}$ above geodesy marker DR9599. The relativistic red shift due to the elevation of the Ramsey cavity

above the marker is

$$\frac{\Delta f}{f} = \frac{h_m g}{c^2}, \quad (4)$$

where $g = 9.79602373(4) \text{ m s}^{-2}$ is the magnitude of the gravitational acceleration measured at the DR9599 geodesy marker [21]. The fractional frequency shift due to the elevation of the Ramsey cavity above the marker is 2.12×10^{-16} , with an uncertainty of 5×10^{-19} relative to the marker.

The combined fractional frequency shift due to the relativistic red and second-order Doppler shifts for an atomic cloud launched to a height $h_a = 0.326(5) \text{ m}$ above the mid-plane of the Ramsey cavity can be expressed as [36]:

$$\frac{\Delta f}{f} = \frac{h_a g}{3c^2}. \quad (5)$$

For NIST-F4, this shift is 0.12×10^{-16} with an uncertainty of 2×10^{-19} relative to the mid-plane of the Ramsey cavity.

The fractional frequency correction for the relativistic red and second-order Doppler shifts for NIST-F4 is the sum of the three contributions given above, $1809.59(1) \times 10^{-16}$, and is given in table 2.

4.4. Cold collision frequency shift

Collisions between Cs atoms during the fountain sequence cause a frequency shift that is proportional to the density of the cloud, where the magnitude depends on the collision energy and its evolution during the Ramsey interrogation [37–40]. The shift is measured during a fountain evaluation by alternating high- and low-density operation. In the low-density mode, a mechanical shutter blocks the molasses repumping laser beam for the first half of the loading phase, with the rest of the fountain cycle the same as for the high-density mode. From the measured frequencies and atom numbers in the high- and low-density modes, the frequency is extrapolated to the limit of zero-density. The type A uncertainty of the fountain frequency evaluation includes the statistical uncertainty due to the zero-density extrapolation.

For high-density operation, the cold collision shift is typically less than 1×10^{-15} . Experiments with different atom number ratios between the high- and low-density modes were performed. The results were consistent with the linear extrapolation within the statistical uncertainty of the measurements. We analyzed the values of the transition probability measured in high- and low-density modes of operation. A significant systematic difference in the transition probabilities would indicate a change in the local density distribution, since the atom cloud extends spatially away from the Ramsey cavity axis, where the microwave amplitude changes non-linearly away from the axis. The measured transition probability between high- and low-density modes changes by less than 0.2%, indicating no significant cloud local density change in the transverse plane. Measurements of the time-of-flight signals in

high- and low-density modes of operation [11, 29] reveal no systematic differences in the signal shapes above 1%, also indicating that the cloud local density does not change significantly along the vertical direction. As a conservative estimate, a 10% systematic uncertainty is added to the measured collisional shift to account for a possible non-linearity between the actual cloud density and measured atom number. Typical corrections for the cold collision shift and its systematic uncertainty are given in table 2.

4.5. Distributed cavity phase (DCP) frequency shift

DCP frequency shifts arise from spatial phase variations in the microwave field of the fountain's Ramsey cavity, which are ultimately a result of power losses on the cavity walls and endcaps. It has become standard to describe the DCP variations as a Fourier series in $\cos(m\phi)$ and $\sin(m\phi)$, where m is an integer and ϕ is the azimuthal angle [41–43]. If each atom perfectly retraced its trajectory through the fountain, the spatial variations of the cavity field would not cause a frequency shift. Due to the non-zero cloud temperature, there is always a horizontal spread of atomic trajectories and a corresponding distribution of frequency shifts due to the spatial phase and amplitude variations of the microwave field [43]. In this section, the three potentially significant DCP Fourier components, $m \leq 2$, are evaluated and included in the uncertainty budget of NIST-F4.

The DCP frequency shifts depend on the distribution of the atoms and the trajectories they follow during the fountain sequence. Several experiments have been done to characterize the distribution of the atoms in NIST-F4. The fraction of atoms that return from the launch has been studied as a function of the launch height. The Rabi oscillations in the Ramsey cavity have been studied as a function of microwave power [43, 44]. The residual excitation of the transitions from $m_F = 0$ to $m_F = \pm 1$ has been studied [45]. Finally, absorption images have been taken of the distribution at several times during the ballistic flight [46]. These investigations have shown that the detected atom population in NIST-F4 can be approximately described as a Gaussian cloud with an initial $1/\sqrt{e}$ radius $\sigma = (3 \pm 1)$ mm and temperature $T = (0.4 \pm 0.1)$ μ K. The transverse temperature is cold enough that the descending cloud does not uniformly fill the aperture of the Ramsey cavity, which has been verified with absorption imaging. These measurements also show that the initial distribution is not fully described by a Gaussian cloud. There could be a bimodal atom cloud velocity distribution, which leads to an inferred temperature of the detected cloud approaching the recoil limit. These details of the initial distribution do not contribute significantly to the uncertainty budget and are neglected here.

The fountain detection system may also affect the DCP frequency shifts if there are spatial variations in the collection of the atomic fluorescence. To bound these effects, we consider a nominally homogeneous detection and a distribution of possible detection inhomogeneities parameterized by a Gaussian spatial dependence with a $1/\sqrt{e}$ radius as small

as 3 mm. Measurements of the detected signals with a slit scanned across the detection beam and the collection lens yield this lower bound on the detection homogeneity.

4.5.1. $m = 0$ DCP component. The endcaps create longitudinal phase variations in the cavity, which lead to a microwave power-dependent shift. The azimuthally symmetric phase variations are described by the $m = 0$ component of the DCP Fourier series [42, 43]. Figure 5 compares the calculated $m = 0$ DCP shift (blue curve) with measurements of the frequency offset of NIST-F4 as a function of microwave amplitude b . The value of $b = 1$ corresponds to a microwave field amplitude that produces a $\pi/2$ average pulse area for a cloud with uniform transverse density distribution passing through the Ramsey cavity [43]. The DCP shifts are expressed as a transition probability asymmetry $\delta P = (\delta P^+ - \delta P^-)/2$, where the transition probabilities δP^\pm are at frequency detunings $\pm \Delta\nu/2$ of the Ramsey fringe, with $\Delta\nu$ the FWHM of the fringe [44]. The calculated $m = 0$ DCP shift uncertainty from the fountain parameter uncertainties is indicated by the shaded region in figure 5.

The DCP $m = 0$ fractional frequency shift at normal operating power is $0.05 \begin{pmatrix} -0.02 \\ -0.07 \end{pmatrix} \times 10^{-16}$, where the uncertainty is due to fountain parameter uncertainties. This correction is included in table 2. A possible unintended difference in the conductivity of the endcaps of $\pm 5\%$ is also considered [43, 44, 47, 49, 50]. At normal operating power, this leads to an uncertainty of 0.02×10^{-16} . Adding the uncertainties due to potential conductivity inhomogeneities and fountain parameters in quadrature gives an $m = 0$ DCP uncertainty of $0.05 \begin{pmatrix} +0.02 \\ -0.08 \end{pmatrix} \times 10^{-16}$, which is included in table 2.

4.5.2. $m = 1$ DCP component. The $m = 1$ DCP variation corresponds to power flow from the microwave feeds across the cavity. If an atom moves across the cavity during the Ramsey free evolution period, it will experience a first-order Doppler shift. The $m = 1$ DCP shift is suppressed in two ways. First, power is supplied to the Ramsey cavity from feeds on opposite sides of the cavity [42, 51]. If the cavity is driven symmetrically, there are no $m = 1$ phase gradients. Second, the fountain and the launch direction can be aligned so that there is no average displacement between the two Ramsey interactions. If the initial cloud is centered on the fountain axis and the fountain is vertical, this corresponds to launching the cloud vertically.

To investigate potential cloud displacements, $m = 1$ DCP shifts can be exaggerated by alternately feeding the cavity with opposing feeds and measuring the frequency difference. The desired launch condition is the fountain tilt for which there is no frequency shift for opposing feeds [44]. The frequency shifts between opposing feeds for both axes of NIST-F4 are shown in figure 6.

In normal operation, the fountain is aligned to minimize the $m = 1$ shift based on the results in figure 6, and the Ramsey

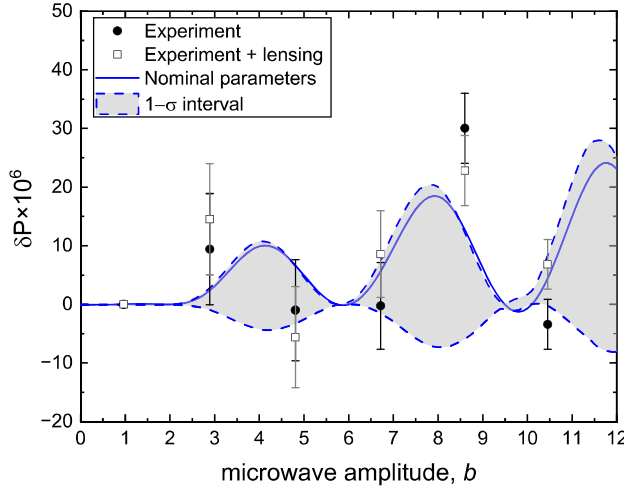


Figure 5. Transition probability difference, δP , as a function of microwave amplitude, b , in the Ramsey cavity, measured (solid symbols) and calculated (blue curves). The shaded region indicates the uncertainty in the predicted $m = 0$ DCP shift due to the uncertainty in the fountain parameters. The measured data corrected for the calculated power dependence of the microwave lensing shift [7, 47, 48] is also shown (open symbols). The measurements were performed at microwave amplitudes that maximized the transition probability on-resonance ($\sim n\pi/2$ pulses for $n = 1, 3, 5, 7, 9$, and 11). For each case, the value of δP at $\pi/2$ pulse area ($b \approx 1$, normal operating condition) is subtracted.

cavity is driven by all four feeds simultaneously. The amplitudes of the feeds were adjusted to make the transition probability as a function of microwave power (Rabi flopping) for each individual feed as symmetric as possible [25, 44]. To assess any remaining $m = 1$ phase gradients, the fountain tilt sensitivity was measured along both axes with all four feeds active, as shown in figure 7. The fractional frequency tilt sensitivity with symmetric, balanced feeding is $(1.1 \pm 0.9) \times 10^{-16} \text{ mrad}^{-1}$ in the X- and $(0.0 \pm 1.0) \times 10^{-16} \text{ mrad}^{-1}$ in the Y-tilt direction. Since the fountain is aligned vertically using single-feed measurements, there is no $m = 1$ DCP bias. As a conservative estimate, a tilt uncertainty of $\pm 1 \text{ mrad}$ is assigned. This tilt uncertainty combined with the measured residual tilt sensitivity leads to an uncertainty for the $m = 1$ DCP shift in the X- and Y-axes of 1.4×10^{-16} and 1.0×10^{-16} , respectively. These are combined in quadrature to give an $m = 1$ DCP uncertainty of 1.7×10^{-16} , which is included in table 2. The 1 mrad tilt uncertainty is included in the fountain parameter uncertainties of the $m = 0$ and $m = 2$ DCP shifts.

It is also interesting to compare the measured differential tilt sensitivity for a single unbalanced feed to the calculations. In figure 6, the differential tilt sensitivity is $(4.9 \pm 1.5) \times 10^{-16} \text{ mrad}^{-1}$ for the X direction and $(9.9 \pm 1.4) \times 10^{-16} \text{ mrad}^{-1}$ for the Y direction. The calculated differential tilt sensitivity is $16.1 \times 10^{-16} \text{ mrad}^{-1}$. The modeled tilt sensitivity is significantly larger than the measured tilt sensitivity. The excitation of the $m = 1$ DCP gradients

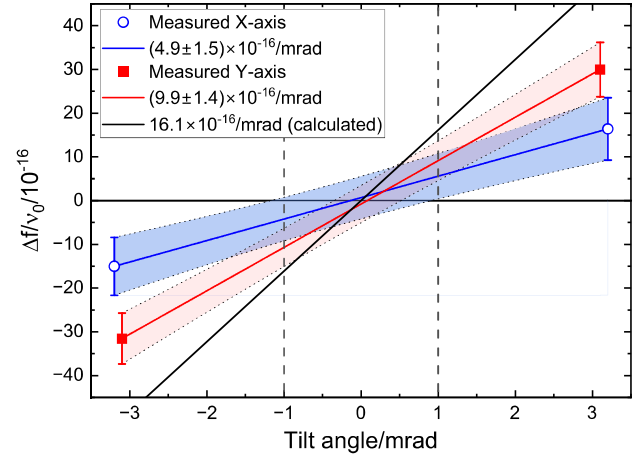


Figure 6. Differential fractional frequency shift between opposing feeds as a function of fountain tilt for both axes of NIST-F4. Solid lines show the best fit slope to the measured fractional frequency shifts (red, blue lines) and the calculated $m = 1$ DCP fractional frequency shifts (black line). Shaded regions indicate the uncertainty in the best-fit slopes ($1-\sigma$ confidence interval). For normal operation, the fountain is aligned so that there is no frequency shift between opposing feeds. Vertical dashed lines indicate the estimated uncertainty in the alignment of the fountain. For this measurement campaign, the tilt of NIST-F4 was alternated every few days. A second Cs fountain, NIST-F3 [52], was used as a reference to correct for the drift of the hydrogen maser reference of the microwave synthesis chain.

can be highly sensitive to the dimensions of the mode filters used to detune the TM_{111} mode from the TE_{011} mode [43]. The discrepancy between measured and modeled tilt sensitivities may be due to uncertainties in the mode filter dimensions, although the measured nearby $m = 1$ mode was well detuned, as expected.

The $m = 1$ DCP term is the dominant uncertainty in NIST-F4's error budget. In future work, this uncertainty could be reduced with more stringent constraints on the alignment of the fountain or by reducing the residual tilt sensitivity by fine-tuning the balance of the feeds [44].

4.5.3. $m = 2$ DCP component. The $m = 2$ DCP shift corresponds to quadrupolar phase variations around the cavity axis. Typically, $m = 2$ shifts can be significant if the cloud is offset on the first passage through the Ramsey cavity or if a detection beam is aligned along a feed axis, which allows detection inhomogeneities to produce an $m = 2$ DCP shift [43]. In NIST-F4, the $m = 2$ DCP shift is suppressed in two ways. First, excitation of the $m = 2$ mode is suppressed by driving the cavity symmetrically with four balanced feeds. Second, the detection beam is oriented at 45° to the feeds of the Ramsey cavity so that any residual excitation of the $m = 2$ mode is averaged by the detection system.

Even with this suppression, an $m = 2$ DCP shift can remain in NIST-F4 if the initial cloud is offset from the fountain axis.

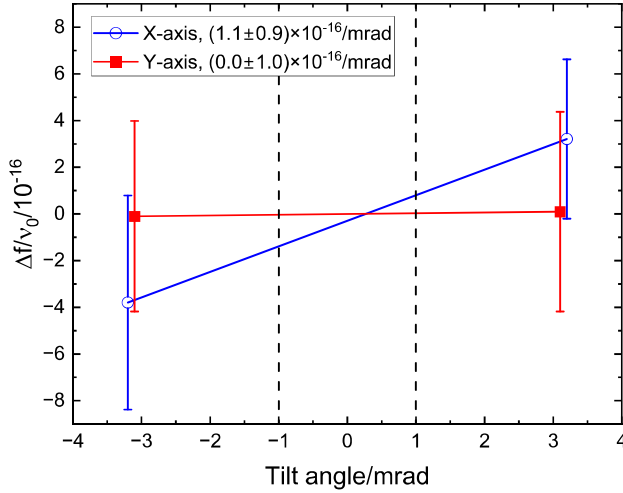


Figure 7. Fractional frequency shift with four active feeds versus fountain tilt in two orthogonal directions. Vertical dashed lines indicate the ± 1 mrad tilt uncertainty used to estimate the $m = 1$ DCP uncertainty. NIST-F3 was used as a reference to correct for the drift of the hydrogen maser reference of the microwave chain. A frequency offset between the two fountains due to an unknown frequency shift in NIST-F3 was subtracted from the data.

To bound this error, the case where the cloud offset has a 2 mm uncertainty and the cavity is excited from only two feeds is modeled so that the $m = 2$ mode is not suppressed. Absorption images show that the offset between the cloud and the cavity center is less than 2 mm [46].

With four-feed operation, the $m = 2$ shift is suppressed to the extent the feeds are balanced. Based on the difference in the residual tilt sensitivity between the X- and Y-axes with all four feeds active, we estimate that our feed balancing procedure suppresses the $m = 2$ DCP sensitivity by at least a factor of 0.3. Combining this suppression factor with the fountain parameter uncertainties, the calculated $m = 2$ DCP uncertainty is 0.20×10^{-16} in fractional frequency units, and is included in table 2.

4.6. Microwave lensing shift

Spatial variations in the microwave field in the Ramsey cavity act as a lens on the atomic wave function [48, 53]. The lensing combines with the apertures along the fountain axis to more selectively attenuate one of the two dressed states and produce a frequency shift. A full treatment of the lensing shift is given in references [7, 47]. The shift depends on the cloud parameters and the apertures in the fountain geometry. For NIST-F4, the restrictive aperture is below the state-selection cavity with a radius of 5 mm as shown in figure 1. The calculated lensing fractional frequency shift is $(0.9^{+0.2}_{-0.4}) \times 10^{-16}$ and is applied to NIST-F4's frequency. The uncertainty in the correction is due to the fountain parameter uncertainties, $(^{+0.07}_{-0.33}) \times 10^{-16}$, and neglected higher-order terms in the theory, (0.2×10^{-16}) [7], which are added in quadrature.

5. Additional systematic uncertainties

5.1. AC Stark (light) shifts

Stray light from the laser system can produce an AC Stark shift of the clock transition during the Ramsey interrogation. To prevent this, mechanical shutters block the inputs of the optical fibers delivering light to the fountain optical table as shown in figure 2 [20]. Each fiber input is blocked by two shutters for redundancy. The power attenuation of each mechanical shutter is at least 40 dB. The measured light shift in NIST-F4 with open shutters for the molasses cooling and repumper beams is $49(1.5) \times 10^{-15}$ in fractional frequency units. Attenuating this light shift by 40 dB (single-shutter) results in a residual light shift of approximately 5×10^{-19} . As an upper limit, a light shift uncertainty of 1.0×10^{-18} is assigned and included in table 2.

It is also possible for scattered light from the lasers to reach the atoms and potentially cause an AC stark shift. In order to minimize scattered light, enclosures have been built around the optics on the laser table. The laser and fountain optical tables are also surrounded by safety curtains. Finally, the frequency of the Ti:Sapphire laser is 172.25 MHz red-detuned from the $|6^2S_{1/2}(F=4)\rangle \rightarrow |6^2P_{3/2}(F'=5)\rangle$ optical transition, which reduces the possible light shifts.

5.2. Background gas collisions

Collisions between cold Cs atoms and the background gas in the vacuum chamber produce frequency shifts in atomic fountains [54]. These shifts can be quantified by measuring the cold atom loss as a function of the background pressure [54, 55].

The UHV of NIST-F4 is maintained by a combination of ion and non-evaporable getter (NEG) pumps. The residual pressure in the molasses loading zone is below 1.5×10^{-8} Pa, measured with an extended-range ion gauge. To estimate the frequency shift due to residual background gas collisions, the returned atom number fraction at zero pressure was determined by measuring the atom cloud fluorescence in the detection zone on the atoms' ascent and descent as a function of the residual vacuum pressure measured by the ion gauge. The pressure was changed by elevating the temperature of the NEG pumps (thus releasing hydrogen) and allowing the H_2 pressure to stabilize. The pressure was varied between 1.5×10^{-8} Pa and 3.8×10^{-7} Pa. Over this pressure range, the returned atom number fraction varied between 8.1% and 1.5%. By extrapolating to the limit of zero background gas pressure, the estimated atom loss at nominal pressure due to H_2 collisions is below 1%.

The loss of cold atoms due to collisions with hot cesium atoms was estimated by measuring the returned atom fraction as a function of the cesium background density. Increasing the temperature of the cesium ampoule yielded twice the cesium fluorescence signal in the molasses zone with a corresponding decrease of the returned atom fraction from 8.0(0.2)%

to 7.6(0.4)%. From these measurements, the estimated atom number loss at nominal warm cesium densities due to collisions with hot cesium atoms is below 1%.

From [54], the fractional frequency shift due to background gas collisions is

$$\Delta\nu/\nu_0 = -\Delta A / (13.8\pi\nu_0 T_R) \Delta C_6/C_6, \quad (6)$$

where ΔA is the fractional number loss, ν_0 is the frequency of the clock transition, $T_R \approx 0.5$ s is the Ramsey time, and $\Delta C_6/C_6$ describes the van der Waals interaction between the background gas and the Cs ground state components. $\Delta C_6/C_6$ is approximately 1/34000 for hydrogen and 1/25000 for cesium [54]. With $\Delta A = 1\%$, the frequency shifts from background collisions between hydrogen and cesium are at the 2×10^{-18} level. The two contributions are combined in quadrature to place an upper limit on the uncertainty due to background gas collisions at 3×10^{-18} .

5.3. Rabi and Ramsey pulling

The Rabi and Ramsey pulling frequency shifts result from the magnetically sensitive microwave transitions in the Cs ground state manifold, which are separated from the clock transition by the C-field. Microwave transitions with $m_F \neq 0$, $\Delta m_F = 0$ can produce asymmetries in the transition probability baseline, leading to Rabi pulling [56]. Microwave transitions with $\Delta m_F = \pm 1$ that involve the $m_F = 0$ clock state may produce Ramsey pulling, which is described in detail for thermal beam clocks in [57], and for fountain clocks in [45].

An upper estimate of the fractional frequency shift due to Rabi pulling can be obtained from measurements of the asymmetry of the amplitudes of the two $m_F = \pm 1$, $\Delta m_F = 0$ microwave transitions [57]. The maximum excitation probability for these transitions was less than 1% for both transitions, with no asymmetry between the two transitions within the measurement uncertainty of 0.2%. The microwave power for these experiments was essentially the same as in normal fountain operation because the ratio of the Rabi frequencies of the $m_F = 0 \rightarrow m_F = 0$ clock transition and the magnetically sensitive $m_F = \pm 1 \rightarrow m_F = \pm 1$ transitions is $4/\sqrt{15} \approx 1.03$.

The fractional frequency shift due to Ramsey pulling can be enhanced in the presence of asymmetric atomic superpositions involving an $m_F = 0$ clock state and the magnetically sensitive $m_F = \pm 1$ states [45]. Asymmetric superpositions can be generated if the state-selection microwave synthesizer is detuned from the clock transition. For NIST-F4, the state-selection synthesizer output frequency is set to resonance and the amplitude is set to a π -pulse area for the clock transition to minimize any possible asymmetric atomic superpositions.

The combined fractional frequency shift due to Rabi and Ramsey pulling for NIST-F4 was calculated using the model described in [45]. With a bias magnetic field of approximately 170 nT, measured fractional populations of the $m_F = \pm 1$ states below 1% and symmetric around $m_F = 0$, and the absence of coherent effects, the combined shift for these systematic errors

is below 1.0×10^{-17} , which is taken as a systematic uncertainty and included in table 2.

5.4. Microwave modulation and spurious components

Treatments of spurious modulation components in the microwave spectrum of continuously-running Cs beam clocks have shown that frequency shifts can occur if a spurious modulation component coincides with the modulation frequency for synchronous resonance detection, or if the modulation sidebands are asymmetric [58, 59]. For pulsed systems, like atomic fountains, asymmetric modulation sidebands lead to an asymmetry in the Ramsey fringe, which causes a second-order frequency shift, similar to the case of a continuous clock [60]. In the case of pulsed systems, symmetric modulation sidebands can cause a first-order frequency shift if the modulation frequency is synchronous with the clock cycle [60].

To quantify any potential bias due to spurious modulation of the microwave signal used in the Ramsey interrogation, the output spectrum of the microwave synthesizer was investigated in detail. For frequency detunings larger than 1 kHz, the only measured spurious spectral components were at 9.2 GHz and $9.207368 \text{ GHz} = 9.2 \text{ GHz} + 7.368 \text{ MHz}$. These two signals are unwanted outputs from the single-sideband mixer that is used in the synthesizer. These tones are -26 dB and -23 dB below the 9.192 GHz signal, respectively. The frequency shift resulting from these signals is negligible due to their large frequency detuning from the atomic resonance.

For frequency detunings less than 1 kHz, the phase (PM) and amplitude (AM) noise spectra of the NIST-F4 microwave synthesizer at 9.192 GHz carrier frequency are shown in figure 8. In the AM spectra, there are no modulation sidebands above -110 dBc Hz^{-1} in this frequency range. At 60 Hz, the AM noise spectrum is below -135 dBc Hz^{-1} . A single sideband with -135 dBc power at 60 Hz could lead to a first-order fractional frequency shift of 2×10^{-17} if the fountain were operated with a cycle duration synchronous with the 60 Hz modulation [60].

For the PM spectra, the only detected spurious modulation with a frequency below 1 kHz is at 60 Hz and has a single sideband power of -66 dBc . This 60 Hz PM modulation could lead to a fractional frequency shift as large as 3×10^{-15} , again if the fountain were operated synchronously with the 60 Hz modulation.

The frequency shifts caused by 60 Hz AM and PM modulation are suppressed in NIST-F4 by using a fountain cycle time corresponding to an $(N + 1/4)$ 60 Hz-periods, where N is an integer [29, 61]. With the timing board referenced to a NIST hydrogen maser, the first-order shift due to the 60 Hz modulation is suppressed to better than 1% by averaging over many cycles. A conservative uncertainty of 3×10^{-17} is assigned for imperfect averaging of this shift by the fountain cycle time.

A frequency shift can also occur if there is a perturbation to the phase of the synthesizer's output that is synchronized with the fountain cycle [62]. To probe possible synchronous phase transients in NIST-F4, a second 9.2 GHz DRO was mixed with

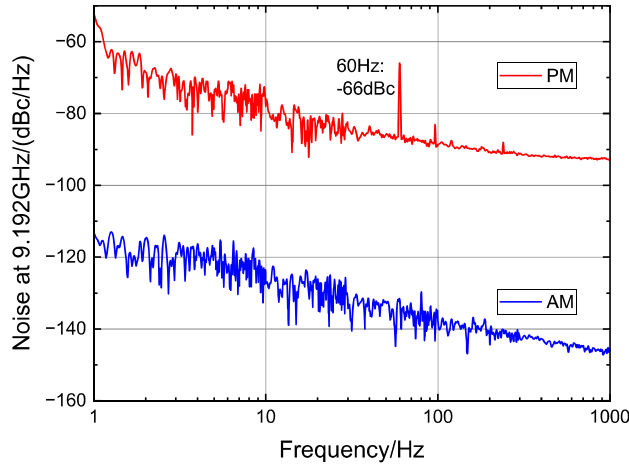


Figure 8. Phase (PM, red curve) and amplitude (AM, blue curve) noise of the NIST-F4 microwave synthesizer.

the output of the synthesizer that was set to 9.196 GHz. Both the synthesizer and the auxiliary DRO were referenced to the same 100 MHz source. The 4 MHz beat frequency between the auxiliary DRO and the synthesizer was measured synchronously with the fountain cycle by triggering a digital lock-in amplifier [62, 63]. The lock-in amplifier was referenced to a 10 MHz signal phase-locked to the 100 MHz reference used for the DROs.

The microwave phase as a function of time after the atoms are launched, averaged over 3×10^5 fountain cycles, is shown in figure 9. The measurements were done using the normal fountain cycle. During each cycle, FSK modulation is applied to the Ramsey DDS to suppress possible frequency shifts due to microwave leakage. The FSK detuning of the Ramsey DDS was disabled at the beginning of the molasses loading phase, 250 ms before the launch trigger marking the time axis origin in figure 9. The blue (red) region in figure 9 highlights the microwave signal phase during the first (second) Ramsey interaction. Averaging over the highlighted regions gives a phase difference of $0.72 \mu\text{rad}$, which corresponds to a fractional frequency error of 0.24×10^{-16} . The origin of the slow phase variation in figure 9 is not known, and it is unlikely to be stable over time. As a conservative estimate, we assign an uncertainty of 0.34×10^{-16} , which corresponds to a phase shift of $1 \mu\text{rad}$ between the two Ramsey interactions. Adding the uncertainties due to synchronous phase transients and imperfect averaging of the frequency shift due to the 60 Hz modulation in quadrature gives an uncertainty for microwave modulation of 0.5×10^{-16} , which is included in table 2.

5.5. Microwave leakage

Frequency shifts can occur if the atoms interact with a resonant microwave field outside of the Ramsey cavity [24, 56, 64]. In a fountain clock, microwave leakage frequency shifts are suppressed due to the reversal of the atomic trajectories.

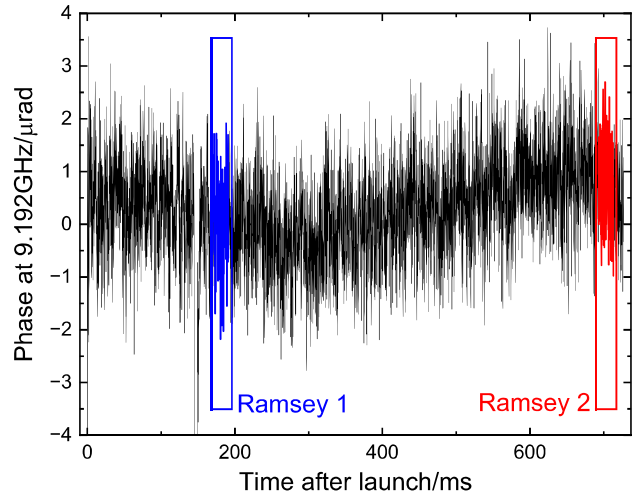


Figure 9. Microwave phase as a function of time after launch. The time interval corresponding to the first (second) Ramsey interaction is indicated by the blue (red) region.

However, if the leakage field has temporal or spatial variations, a frequency shift can occur. It is useful to categorize possible leakage shifts according to when the atoms interact with the unwanted field [24, 64].

We suppress shifts due to leakage before the first Ramsey interaction with the following mechanisms. First, the state-selection microwaves are detuned using FSK modulation. Second, during the state-selection, a laser beam removes all atoms from the $|F=4\rangle$ ground state component and thereby any coherent effect from a possible microwave interaction shortly before the first Ramsey interaction. Also, after the state-selection, the atoms enter a below-cutoff section between the state-selection and Ramsey cavities, where the microwave field is attenuated and the potential interaction time is short. Shifts due to a leakage field above the Ramsey cavity are suppressed by a below-cutoff drift tube, which attenuates any microwave field above the Ramsey cavity by a large factor [4, 6].

The most likely source of a microwave leakage shift in NIST-F4 is a leakage field after the second Ramsey interaction, especially in the state-selection cavity and below it. To suppress this possibility, both the state-selection and Ramsey microwave synthesizers are detuned using FSK modulation after the second Ramsey interaction.

Measurements of δP as a function of microwave amplitude can also be used to estimate the suppression of microwave leakage below the Ramsey cavity [11, 24]. The measurements have to be corrected for the $m=0$ DCP and microwave lensing frequency shifts [7, 11, 43, 47, 53]. Residual leakage below the Ramsey cavity produces a shift of the form $\delta P = \alpha \Omega \sin \Omega$, where Ω is the pulse area for a single-cavity passage and α is determined from the data [11, 24]. This analysis is applied to the results of figure 5. The uncertainty in the $m=0$ DCP shift is added in quadrature to the measurement uncertainties. The

estimated fractional frequency shift due to microwave leakage at normal power is $0.4(0.3) \times 10^{-16}$ without the correction due to lensing and $-0.20(0.3) \times 10^{-16}$ when the correction due to lensing is included. An uncertainty of 0.4×10^{-16} is assigned for microwave leakage and included in table 2.

5.6. Cavity pulling

Cavity pulling shifts occur when there is a detuning between the atomic resonance and the TE₀₁₁ mode of the Ramsey cavity. In NIST-F4, the temperature of the Ramsey cavity is steered to ensure the TE₀₁₁ mode is resonant with the Cs transition frequency. The measured temperature dependence of the TE₀₁₁ mode is $-0.16(1)$ MHz K⁻¹, leading to a cavity resonance detuning of ± 32 kHz for the measured absolute cavity temperature fluctuations of ± 0.2 K.

The first-order cavity pulling shift due to the presence of oscillating atomic magnetic dipoles has been studied in [61, 65]. Following the formalism in [65], the worst-case fractional frequency shift for ± 100 kHz cavity resonance detuning is 4×10^{-18} for an atom number $N_{\text{at}} = 10^5$, which is larger than the atom number typically used in high-density mode. Since this shift is proportional to the atom number, it is part of the measurement protocol of the cold collision shift, and it is included in the shift correction.

The second-order cavity pulling effect has been studied using the formalism in [56]. From the Ramsey cavity's loaded Q factor given in table 1, a maximum cavity detuning of ± 32 kHz and a maximum pulse area deviation from the nominal $1\pi/2$ value of ± 0.45 dB (5% pulse area variation), the maximum fractional frequency shift is estimated as 1.1×10^{-17} . This is taken as the uncertainty due to cavity pulling and given in table 2.

5.7. Majorana transitions

Majorana transitions in a fountain clock occur when the atoms experience a change of the static magnetic field direction that is fast compared to their Larmor precession frequency, which can occur if the field changes direction or goes to zero [66]. For these transitions to cause a frequency shift, the fountain's detection zone needs to have a sensitivity that depends on the atomic Zeeman state m_F [67].

For NIST-F4, the direction of the magnetic field inside the magnetic shields is the same as the direction of the magnetic field outside. As a result, the atoms do not pass through a region with no magnetic field [67]. Additionally, all detection beams are linearly polarized with an extinction ratio $>10^2$, making the atomic fluorescence detection largely independent of the Zeeman sublevels of the $|F=4\rangle$ and $|F=3\rangle$ states.

To enhance effects due to a possible Majorana transition, the direction of the bias magnetic field was intentionally reversed and the detection system was converted to use circularly polarized light. This configuration produced a fractional frequency shift less than 1×10^{-15} compared to the normal operating state. As a conservative estimate, an uncertainty of

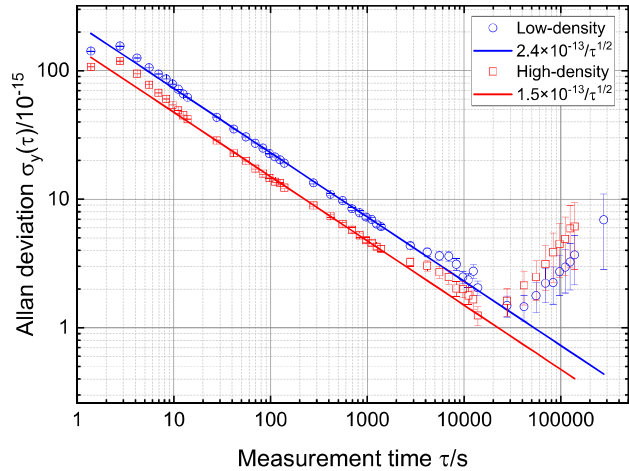


Figure 10. Allan deviation, $\sigma_y(\tau)$, of NIST-F4 versus a hydrogen maser during a 15 days measurement campaign. The frequency drift for $\tau > 10^4$ s is due to the maser.

1.0×10^{-17} is assigned for possible Majorana transitions and included in table 2.

6. Evaluation campaigns and comparisons with other primary standards

Five measurement campaigns of NIST-F4 versus one of NIST's commercial hydrogen masers were performed in the period between Modified Julian Date 60 124 and 60 569. Each campaign covered consecutive 5 days intervals, with typical 15 days duration and $>99\%$ up-time. A typical Allan deviation plot of NIST-F4's fractional frequency stability in high- and low-density modes is shown in figure 10.

Figure 11 shows the results of the five measurement campaigns in which NIST-F4 was compared to the weighted average of all the Primary and Secondary Frequency Standards (PSFS) reporting in the corresponding Circular T report [68] of the Bureau International des Poids et Mesures. The frequency comparison chain for the measurements was NIST-F4 vs NIST maser vs NIST timescale vs TAI vs PSFS. The uncertainties shown in figure 11 are given by the quadratic sum of the statistical uncertainty of NIST-F4 versus the hydrogen maser referencing the microwave synthesis chain, the type B systematic uncertainty of NIST-F4, the dead time uncertainty due to the incomplete overlap between the measurement interval and the Circular T period, and the link uncertainty due to the Two-Way Satellite Time and Frequency Transfer (TWSTFT) used to connect the hydrogen maser frequency to TAI. The extrapolation from 10 days or 15 days to the Circular T month of 30 days or 35 days was done using the NIST time scale as the flywheel. The stability of the NIST timescale was used to calculate the dead time uncertainty, which averaged at 4.7×10^{-16} . NIST-F4 agrees with the PSFS ensemble within the measurement uncertainties.

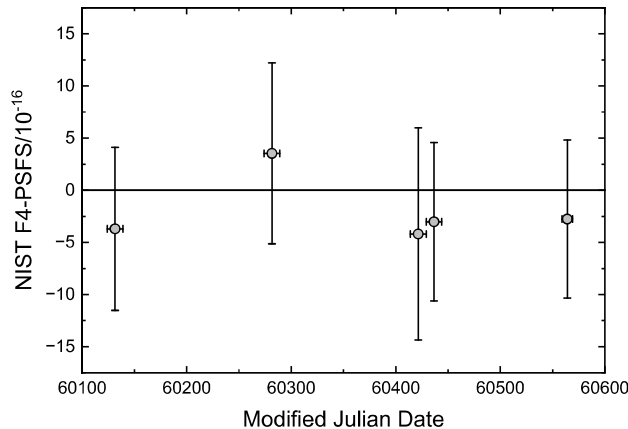


Figure 11. Fractional frequency difference between NIST-F4 and Primary and Secondary Frequency Standards (PSFS) contributing to TAI using data from Circular-T reports.

7. Conclusion

NIST-F4 is an operational PFS with a frequency stability of $\sigma_y(\tau) = 1.5 \times 10^{-13}/\sqrt{\tau}$ in high-density mode of operation, where τ is the averaging time in seconds, and a type B frequency uncertainty $\sigma_B = 2.2 \times 10^{-16}$. During a measurement campaign, the fountain interleaves high-density and low-density modes to measure the collisional shift. After accounting for the interleaved operation, the frequency stability is $\sigma_y(\tau) = 4.6 \times 10^{-13}/\sqrt{\tau}$. For an integration time of 20 d, the statistical (type A) uncertainty is 3.5×10^{-16} . Assuming the collisional shift is stable over long periods, the effective fountain instability without statistical contribution from the collisional shift is $\sigma_y(\tau) \sim 2.0 \times 10^{-13}/\sqrt{\tau}$. This lower statistical instability can be used to study fountain shifts and diagnose problems unrelated to possible variations in the collisional shift.

The fountain's frequency stability is limited by the contributions from the OCXO-based local oscillator phase noise and the fountain quantum projection noise. Both contributions are expected to improve by using a local oscillator with lower phase noise, and by improved cold atom loading, combined with advanced collisional shift measurements [28, 40].

The type B frequency uncertainty is dominated by the uncertainties of the first-order Doppler shift and the cold collision shift. In future work, the $m = 1$ DCP uncertainty may improve with further measurements of the tilt sensitivity and a more accurate vertical alignment of the atomic cloud trajectory. The collisional shift uncertainty could be reduced with more sophisticated state preparation methods [28, 40].

NIST-F4 is expected to provide data for the realization of the time scale UTC(NIST) and for TAI calibrations. The fountain can also support measurements of the absolute frequency of local optical frequency standards, including to support a future redefinition of the SI second [19].

Acknowledgment

This work was funded by NIST, a U.S. government agency. This material is also based (in part) upon work supported by the U.S. National Science Foundation under Award No. 2012117 (KG). The authors thank Craig Nelson, Archita Hati and Marco Pomponio for their help with the fountain local oscillator and microwave synthesizer, and Ying-Ju Wang, Fabrizio Giorgetta, and Kyle Beloy for helpful suggestions on the manuscript.

ORCID iDs

Vladislav Gerginov  <https://orcid.org/0000-0003-0581-8330>

Thomas E Parker  <https://orcid.org/0000-0003-3264-9245>

Kurt Gibble  <https://orcid.org/0000-0003-3652-9638>

Jeff A Sherman  <https://orcid.org/0000-0002-8560-481X>

References

- [1] Primary and secondary frequency standards participating to TAI, since September 2003 (available at: https://webtai.bipm.org/database/show_psfs.html)
- [2] Clairon A, Ghezali S, Santarelli G, Laurent P, Lea S N, Bahoura M, Simon E, Weyers S and Szymaniec K 1996 Preliminary accuracy evaluation of a cesium fountain frequency standard *Proc. 5th Symp. Frequency Standards and Metrology* (World Scientific) pp 45–49
- [3] Weyers S, Hübner U, Schröder R, Tamm C and Bauch A 2001 Uncertainty evaluation of the atomic caesium fountain CSF1 of the PTB *Metrologia* **38** 343–52
- [4] Jefferts S R *et al* 2002 Accuracy evaluation of NIST-F1 *Metrologia* **39** 321
- [5] Abgrall M *et al* 2015 Atomic fountains and optical clocks at SYRTE: status and perspectives *C. R. Phys.* **16** 461–70
- [6] Heavner T P, Donley E A, Levi F, Costanzo G, Parker T E, Shirley J H, Ashby N, Barlow S and Jefferts S R 2014 First accuracy evaluation of NIST-F2 *Metrologia* **51** 174
- [7] Weyers S, Gerginov V, Kazda M, Rahm J, Lipphardt B, Dobrev G and Gibble K 2018 Advances in the accuracy, stability and reliability of the PTB primary fountain clocks *Metrologia* **55** 789
- [8] Szymaniec K, Lea S N, Gibble K, Park S E, Liu K and Głowacki P 2016 NPL Cs fountain frequency standards and the quest for the ultimate accuracy *J. Phys.: Conf. Ser.* **723** 012003
- [9] Takamizawa A, Yanagimachi S and Hagimoto K 2022 First uncertainty evaluation of the cesium fountain primary frequency standard NMJ-F2 *Metrologia* **59** 035004
- [10] Levi F, Calonico D, Calosso C E, Godone A, Micalizio S and Costanzo G A 2014 Accuracy evaluation of ITCsF2: a nitrogen cooled caesium fountain *Metrologia* **51** 270
- [11] Beattie S, Jian B, Alcock J, Gertszvolf M, Hendricks R, Szymaniec K and Gibble K 2020 First accuracy evaluation of the NRC-FCs2 primary frequency standard *Metrologia* **57** 035010

- [12] Fang F, Liu N, Liu K, Chen W, Suo R and Li T 2016 Operation of NIM5 fountain with 1.5×10^{-15} uncertainty and design of new NIM6 in NIM *J. Phys.: Conf. Ser.* **723** 012009
- [13] Acharya A, Arora P, Bharath V, Yadav S, Agarwal A and Gupta A S 2015 Complete uncertainty evaluation of the cesium fountain primary frequency standard: NPLI-CsF1 ATF Workshop
- [14] Kumagai M, Ito H, Kajita M and Hosokawa M 2008 Evaluation of caesium atomic fountain NICT-CsF1 *Metrologia* **45** 139
- [15] Blinov I Y, Boiko A I, Domnin Y S, Kostromin V P, Kupalova O V and Kupalov D S 2017 Budget of uncertainties in the cesium frequency frame of fountain type *Meas. Tech.* **60** 30–36
- [16] Jallageas A, Devenoges L, Petersen M, Morel J, Bernier L G, Schenker D, Thomann P and Südmeyer T 2018 First uncertainty evaluation of the FoCS-2 primary frequency standard *Metrologia* **55** 366
- [17] Wang X-L et al 2023 First evaluation of the primary frequency standard NTSC-CsF2 *Metrologia* **60** 065012
- [18] Guéna J et al 2017 First international comparison of fountain primary frequency standards via a long distance optical fiber link *Metrologia* **54** 348
- [19] Dimarcq N et al 2024 Roadmap towards the redefinition of the second *Metrologia* **61** 012001
- [20] Heavner T P, Jefferts S R, Donley E A, Shirley J H and Parker T E 2005 NIST-F1: recent improvements and accuracy evaluations *Metrologia* **42** 411–22
- [21] Van Westrum D 2024 *National Geodetic Survey Technical Memorandum* NOAA (in preparation)
- [22] Hoth G W, Gerginov V, Gibble K, Green H, Ellzey A, Hagen K, Schwadron C, Uhrich J and Thatcher K 2024 Microwave cavity design for the NIST primary frequency standards (in preparation)
- [23] Heavner T P, Jefferts S R, Donley E A, Parker T E and Levi F 2005 A new microwave synthesis chain for the primary frequency standard NIST-F1 *Proc. 2005 IEEE Int. Frequency Control Symp. and Exposition, 2005* pp 308–11
- [24] Shirley J H, Levi F, Heavner T P, Calonico D, Yu D-H and Jefferts S R 2006 Microwave leakage-induced frequency shifts in the primary frequency standards NIST-F1 and IEN-CSF1 *IEEE Trans. Ultrason. Ferroelectr. Freq. Control* **53** 2376–85
- [25] Gerginov V, Hoth G W, Heavner T P and Sherman J A 2024 Progress towards an accuracy evaluation of NIST-F4 cesium fountain clock 2024 *European Frequency and Time Forum (EFTF)* pp 123–5
- [26] The authors would like to thank Physikalisch-Technische Bundesanstalt in Germany and specifically Dr. Stefan Weyers and Dr. Johannes Rahm for providing us with the fountain control software CSF-Control
- [27] Breit G and Rabi I I 1931 Measurement of nuclear spin *Phys. Rev.* **38** 2082–3
- [28] Wynands R and Weyers S 2005 Atomic fountain clocks *Metrologia* **42** S64
- [29] Gerginov V, Nemitz N, Weyers S, Schröder R, Griebisch D and Wynands R 2009 Uncertainty evaluation of the caesium fountain clock PTB-CSF2 *Metrologia* **47** 65
- [30] Weyers S, Bauch A, Hubner U, Schröder R and Tamm C 2000 First performance results of PTB's atomic caesium fountain and a study of contributions to its frequency instability *IEEE Trans. Ultrason. Ferroelectr. Freq. Control* **47** 432–7
- [31] Itano W M, Lewis L L and Wineland D J 1982 Shift of $^2S_{1/2}$ hyperfine splittings due to blackbody radiation *Phys. Rev. A* **2** 1233–5
- [32] Arimondo E, Inguscio M and Violino P 1977 Experimental determinations of the hyperfine structure in the alkali atoms *Rev. Mod. Phys.* **49** 31–75
- [33] Rosenbusch P, Zhang S and Clairon A 2007 Blackbody radiation shift in primary frequency standards 2007 *IEEE Int. Frequency Control Symp. Joint With the 21st European Frequency and Time Forum* pp1060–3
- [34] Angstmann E J, Dzuba V A and Flambaum V V 2006 Frequency shift of hyperfine transitions due to blackbody radiation *Phys. Rev. A* **74** 023405
- [35] Pavlis N K and Weiss M A 2017 A re-evaluation of the relativistic redshift on frequency standards at NIST, Boulder, Colorado, USA *Metrologia* **54** 535
- [36] Ashby N 2021 Falling atoms (arXiv:2111.08114)
- [37] Tiesinga E, Verhaar B J, Stoof H T C and van Bragt D 1992 Spin-exchange frequency shift in a cesium atomic fountain *Phys. Rev. A* **45** R2671–3
- [38] Gibble K and Chu S 1993 Laser-cooled Cs frequency standard and a measurement of the frequency shift due to ultracold collisions *Phys. Rev. Lett.* **70** 1771–4
- [39] Ghezali S, Laurent P, Lea S N and Clairon A 1996 An experimental study of the spin-exchange frequency shift in a laser-cooled cesium fountain frequency standard *Europhys. Lett.* **36** 25
- [40] Dos Santos F P, Marion H, Bize S, Sortais Y, Clairon A and Salomon C 2002 Controlling the cold collision shift in high precision atomic interferometry *Phys. Rev. Lett.* **89** 233004
- [41] Davies J B, Fernandez F A and Philippou G Y 1982 Finite element analysis of all modes in cavities with circular symmetry *IEEE Trans. Microw. Theory Tech.* **30** 1975–80
- [42] Li R and Gibble K 2004 Phase variations in microwave cavities for atomic clocks *Metrologia* **41** 376
- [43] Li R and Gibble K 2010 Evaluating and minimizing distributed cavity phase errors in atomic clocks *Metrologia* **47** 534
- [44] Guéna J, Li R, Gibble K, Bize S and Clairon A 2011 Evaluation of doppler shifts to improve the accuracy of primary atomic fountain clocks *Phys. Rev. Lett.* **106** 130801
- [45] Gerginov V, Nemitz N and Weyers S 2014 Initial atomic coherences and Ramsey frequency pulling in fountain clocks *Phys. Rev. A* **90** 033829
- [46] Beattie S and Jian B 2023 Characterization of the collisional frequency shift in an atomic fountain clock using absorption imaging *Metrologia* **60** 045004
- [47] Li R, Gibble K and Szymaniec K 2011 Improved accuracy of the NPL-CsF2 primary frequency standard: evaluation of distributed cavity phase and microwave lensing frequency shifts *Metrologia* **48** 283
- [48] Gibble K 2006 Difference between a photon's momentum and an atom's recoil *Phys. Rev. Lett.* **97** 073002
- [49] Weyers S, Gerginov V, Nemitz N, Li R and Gibble K 2012 Distributed cavity phase frequency shifts of the caesium fountain PTB-CSF2 *Metrologia* **49** 82
- [50] Jian B, Beattie S, Alcock A J, Gertszov M and Gibble K 2019 Evaluation of the distributed cavity phase shifts of the NRC-FCs2 fountain primary frequency standard 2019 *Joint Conf. IEEE Int. Frequency Control Symp. and European Frequency and Time Forum (EFTF/IFC)* pp 1–2
- [51] Khursheed A, Vecchi G and DeMarchi A 1996 Spatial variations of field polarization and phase in microwave cavities: application to the cesium fountain cavity *IEEE Trans. Ultrason. Ferroelectr. Freq. Control* **43** 201–10

- [52] Hoth G W, Sherman J A, Radnaev A G, Mitchell P and Gerginov V 2023 NIST-F3, a cesium fountain frequency reference *Proc. 54th Annual Precise Time and Time Interval Systems and Applications Meeting (Long Beach, CA, USA)* pp 183–8
- [53] Gibble K 2014 Ramsey spectroscopy, matter-wave interferometry and the microwave-lensing frequency shift *Phys. Rev. A* **90** 015601
- [54] Gibble K 2013 Scattering of cold-atom coherences by hot atoms: frequency shifts from background-gas collisions *Phys. Rev. Lett.* **110** 180802
- [55] Szymaniec K, Lea S and Liu K 2014 An evaluation of the frequency shift caused by collisions with background gas in the primary frequency standard NPL-CsF2 *IEEE Trans. Ultrason. Ferroelectr. Freq. Control* **61** 203–6
- [56] Vanier J and Audoin C 1989 *The Quantum Physics of Atomic Frequency Standards* (Institute of Physics Publishing)
- [57] Cutler L S, Flory C A, Giffard R P and De Marchi A 1991 Frequency pulling in cesium beam frequency standards due to $\delta m = \pm 1$ (sigma) transitions *Proc. 45th Annual Symp. on Frequency Control* pp 544–53
- [58] Audoin C, Jardino M, Cutler L S and Lacey R F 1978 Frequency offset due to spectral impurities in cesium-beam frequency standards *IEEE Trans. Instrum. Meas.* **27** 325–9
- [59] Schröder R 1991 Frequency synthesis in primary Cs clocks *Proc. 5th European Frequency and Time Forum*
- [60] Shirley J H, Heavner T P and Jefferts S R 2009 First-order sideband pulling in atomic frequency standards *IEEE Trans. Instrum. Meas.* **58** 1241–6
- [61] Fertig C and Gibble K 2000 Measurement and cancellation of the cold collision frequency shift in an ^{87}Rb fountain clock *Phys. Rev. Lett.* **85** 1622–5
- [62] Santarelli G *et al* 2009 Switching atomic fountain clock microwave interrogation signal and high-resolution phase measurements *IEEE Trans. Ultrason. Ferroelectr. Freq. Control* **56** 1319–26
- [63] Kazda M and Gerginov V 2016 Suppression of microwave leakage shifts in fountain clocks by frequency detuning *IEEE Trans. Instrum. Meas.* **65** 2389–93
- [64] Weyers S, Schröder R and Wynands R 2006 Effects of microwave leakage in caesium clocks: theoretical and experimental results *Proc. 20th European Frequency and Time Forum* pp 173–80
- [65] Bize S, Sortais Y, Mandache C, Clairon A and Salomon C 2001 Cavity frequency pulling in cold atom fountains *IEEE Trans. Instrum. Meas.* **50** 503–6
- [66] Majorana E 1932 Atomi orientati in campo magnetico variabile *Nuovo Cimento* **9** 43–50
- [67] Wynands R, Schröder R and Weyers S 2007 Majorana transitions in an atomic fountain clock *IEEE Trans. Instrum. Meas.* **56** 660–3
- [68] BIPM Circular T (available at: <https://www.bipm.org/en/time-ftp/circular-t>)